Evidence for Dirac flat band superconductivity enabled by quantum geometry

https://doi.org/10.1038/s41586-022-05576-2

Received: 24 November 2021

Accepted: 18 November 2022

Published online: 15 February 2023

Check for updates

Haidong Tian[1], Xueshi Gao[1], Yuxin Zhang[1], Shi Che[1], Tianyi Xu[2], Patrick Cheung[2], Kenji Watanabe[3], Takashi Taniguchi[4], Mohit Randeria[1], Fan Zhang[2], Chun Ning Lau[1]✉ & Marc W. Bockrath[1]✉

In a flat band superconductor, the charge carriers' group velocity v_F is extremely slow. Superconductivity therein is particularly intriguing, being related to the long-standing mysteries of high-temperature superconductors[1] and heavy-fermion systems[2]. Yet the emergence of superconductivity in flat bands would appear paradoxical, as a small v_F in the conventional Bardeen–Cooper–Schrieffer theory implies vanishing coherence length, superfluid stiffness and critical current. Here, using twisted bilayer graphene[3–7], we explore the profound effect of vanishingly small velocity in a superconducting Dirac flat band system[8–13]. Using Schwinger-limited non-linear transport studies[14,15], we demonstrate an extremely slow normal state drift velocity $v_n \approx 1{,}000$ m s^{-1} for filling fraction ν between −1/2 and −3/4 of the moiré superlattice. In the superconducting state, the same velocity limit constitutes a new limiting mechanism for the critical current, analogous to a relativistic superfluid[16]. Importantly, our measurement of superfluid stiffness, which controls the superconductor's electrodynamic response, shows that it is not dominated by the kinetic energy but instead by the interaction-driven superconducting gap, consistent with recent theories on a quantum geometric contribution[8–12]. We find evidence for small Cooper pairs, characteristic of the Bardeen–Cooper–Schrieffer to Bose–Einstein condensation crossover[17–19], with an unprecedented ratio of the superconducting transition temperature to the Fermi temperature exceeding unity and discuss how this arises for ultra-strong coupling superconductivity in ultra-flat Dirac bands.

Figure 1a displays the zero-bias longitudinal resistance R versus gate voltage V_{bg} (bottom axis) and filling fraction ν (top axis) for twisted bilayer graphene (tBLG) device D1 with twist angle $\theta = 1.08 \pm 0.02°$ at zero magnetic field $B = 0$. Sharp peaks emerge at carrier density $n = 0$, −1.4, −2.2 and -2.8×10^{12} cm^{-2}, corresponding to $\nu = 0$, −1/2, −3/4 and −1, respectively, in agreement with previous works[6,20,21]. For $-5/8 \le \nu \le -1/2$, superconductivity is observed. The device displays one-sided Landau fans and resetting of the Hall resistance at $\nu = -1/2$ (Extended Data Fig. 1), which are signatures of the so-called 'Dirac revival'[6,20,21], where the effective charge density $\tilde{n}$ crosses zero, and the Fermi level again aligns to a Dirac point. Hence, in the following $\tilde{n}$ is measured from $\nu = -1/2$, as confirmed by Hall density measurements (Extended Data Fig. 2). All data are taken at temperature $T = 0.3$ K unless otherwise specified.

Normal state: Nonlinear transport and low velocity

We first examine the device's non-linear transport in the normal state, obtained at $B = 0.2$ T. Figure 1b,c plot dV/dI versus $\tilde{n}$ and bias current density J, displaying a 'bell'-like feature. The differential resistance is low (less than or equal to 200 Ω) and constant at small bias (blue region), but increases dramatically to a pronounced peak at a critical current J_{cn} before settling to a high-resistance state (5–7 kΩ, green region). For $-1/2 < \nu < -5/8$, J_{cn} increases almost linearly with increasing hole doping. Similar critical current-like behaviour in dV/dI has recently been observed in tBLG with $\theta = 1.23°$, in graphene/BN superlattices, and in graphene constrictions[14]. The peaks arise from the saturation of the charge carriers' normal state drift velocity to a velocity v_n limited by the band structure; at larger current bias, new charge carriers are generated by the Schwinger mechanism/Zener-Klein tunnelling[15,22]: facilitated by graphene's gapless Dirac spectrum, interband tunnelling creates electron–hole pairs and produces a drop in dV/dI[14,15,22]. In a perfectly linear dispersion with energy $E = \hbar v_F k$, where k is the wavevector and $\hbar$ is the reduced Planck's constant, $v_n \approx v_F$. When the band flattens away from the Dirac point as expected for tBLG at higher doping, v_n is a weighted average of charge carriers' velocities and remains close to the Fermi velocity v_F, thereby providing a characteristic measurement of the band velocity. Using these Schwinger-induced features, we measured v_n experimentally for a number of devices near charge neutrality, and plotted the values together with previously measured v_F in literature[3,14,23,24] versus θ (Fig. 1e). Evidently, near the charge neutrality point, the measured

[1]Department of Physics, The Ohio State University, Columbus, OH, USA. [2]Department of Physics, The University of Texas at Dallas, Richardson, TX, USA. [3]Research Center for Functional Materials, National Institute for Materials Science, Tsukuba, Japan. [4]International Center for Materials Nanoarchitectonics, National Institute for Materials Science, Tsukuba, Japan. ✉e-mail: lau.232@osu.edu; bockrath.31@osu.edu

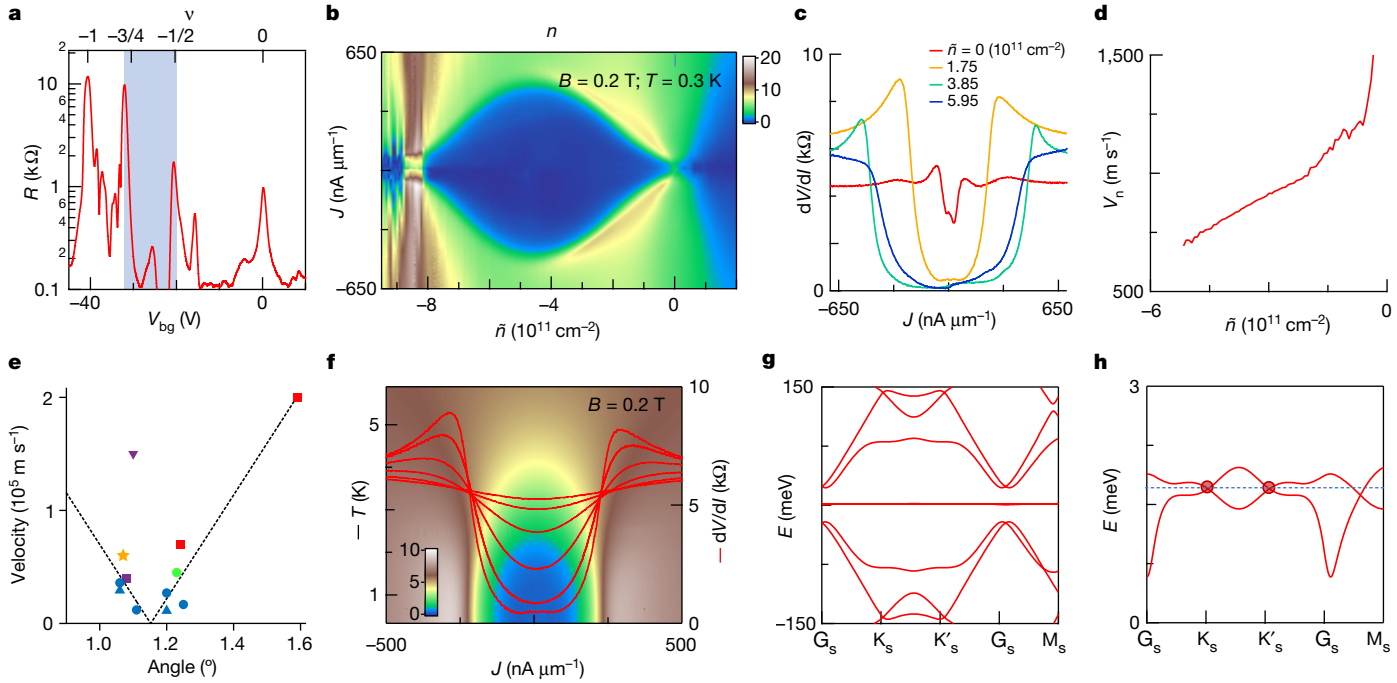

Fig. 1 | Normal state transport of tBLG with θ = 1.08° at B = 0.2 T and T = 0.3 K (unless specified otherwise). a, Log plot of longitudinal resistance R versus V_{bg} (bottom axis) and filling fraction ν (top axis) at B = 0. The shaded region is the range of density that we focus on. **b**–**c**, dV/dI (J, $\tilde{n}$) in kΩ, and line traces at different $\tilde{n}$. **d**, Extracted v_n versus $\tilde{n}$. **e**, Plot of Fermi velocity versus twist angle, for various methods of measurement and from literature. Squares: measured by Shubnikov de Haas (SdH) oscillations; upright triangles: quantum Hall data; star: from chemical potential versus density; inverted triangle: from capacitance; circles: from Schwinger mechanism. Colours indicate data source from various references. Red: ref. [23]; purple: ref. [3]; orange: ref. [24]; green: ref. [14]; blue: data from present study. Dashed lines are fits to data $v = |a(\theta - \theta_{MA})|$, where the moiré period $a = 4.6 \times 10^5$ m s^{-1} per degree (°) and the magic twist angle θ_{MA} = 1.15°, showing the general agreement among the different measurement techniques. The purple inverted triangle is excluded from the fit due to the reported sensitivity of the capacitance data to geometric capacitance, as well as its clear position as an outlier. **f**, dV/dI (J, T) and line traces at $\tilde{n} = -1.75 \times 10^{11}$ cm^{-2}, showing the smearing of the peaks with temperature. Line traces (right axis) are taken at T = 0.34 K, 2 K, 3 K, 4 K, 5 K and 5.8 K, respectively. **g**–**h**, Computed band structure of tBLG with θ = 1.08° and $v_n \approx 1{,}000$ m s^{-1} near the mini-Dirac points. Only one spin-valley species is shown for simplicity. In **h**, the dashed line corresponds to ν = 0, and the red dots denote the mini-Dirac points.

v_n values are consistent with other methods of v_F measurement, confirming the results of ref. [14].

Having tested the non-linear transport technique for measuring the characteristic band velocity, we apply it for $-1/2 < \nu < -5/8$ in device D1. Strikingly, near half-filling, $J_{cn} \approx 70$–500 nA μm^{-1}, more than two orders of magnitude smaller than that reported previously[14], indicating that θ is very close to the magic angle θ_{MA}. Using $v_n = J_{cn}/\tilde{n}e$, where e is electron charge, we obtain $v_n \approx 700$–$1{,}200$ m s^{-1} (Fig. 1d, left axis). This extremely slow velocity is reduced from v_F in monolayer graphene by three orders of magnitude, indicating a small Fermi energy, $E_F \approx \hbar v_n k_F \approx 0.1$ meV, at $\tilde{n} = 10^{-11}$ cm^{-2}, where k_F is the Fermi wavevector of the electrons, constituting the flattest minibands reported to date. This is further confirmed by T-dependent measurements: when $k_B T$ is comparable to the bandwidth, where k_B is the Boltzmann constant, thermal excitation of electron–hole pairs smears the transition from regular to Schwinger-dominated transport, suppressing the dV/dI peaks[14] (Fig. 1f and Extended Data Fig. 3). Our band structure calculations verify that $v_F \approx 1{,}000$ m s^{-1} is reached at mini-Dirac points in devices with θ = 1.08° (Fig. 1g,h).

The above estimate of E_F is justified by v_n being an average of the band velocity over the relaxed Fermi surface in the moving frame of the non-equilibrium current-carrying state, and confirmed by an in-depth analysis of a realistic tBLG band structure that demonstrates at most a modest (30%) deviation of v_n from v_F (Extended Data Figs. 4 and 5). Notably, the velocity near half-filling is characteristically much lower than that near charge neutrality, consistent with previous works[3,4,14]. The astonishingly slow velocity observed is likely associated with θ being extremely close to θ_{MA}; in principle, even slower velocity (down to $v_F = 0$) can be reached if θ is exactly θ_{MA}. While disorder such as angular domains, impurities and strains might be present, the low normal state resistivity indicates that such disorder does not dominate transport and cannot possibly give rise to this extremely slow velocity (see Supplementary Information).

Violation of BCS relations

After establishing the ultra-flat band, we now focus on transport data at B = 0. Superconductivity is observed at $-3.5 < \tilde{n} < 0.3 \times 10^{11}$ cm^{-2}, with a characteristic dome in the T–$\tilde{n}$ plane (Fig. 2a,b). In two dimensions (2D), the superconducting transition is a Berezinskii–Kosterlitz–Thouless transition, driven by vortex–anti-vortex pair proliferation above a critical temperature T_c[25,26]. Empirically we define T_c to be the temperature at which R first exceeds 20% (50%) of the normal state resistance at zero bias, which reaches approximately 2.2 K (3.0 K) at the top of the dome, $\tilde{n} \approx -1.8 \times 10^{11}$ cm^{-2}, taken to be the optimal doping point. This is among the highest reported T_c for tBLG. Following the convention of cuprates, we denote regions with charge density to the right (left) of optimal doping as underdoped (overdoped).

Similarly, a superconducting dome is observed versus B and $\tilde{n}$ (Fig. 2c,d), where the upper critical magnetic field B_{c2} reaches as high as around 0.1 T at optimal doping (Fig. 2e, left axis). Thus, the superconducting coherence length $\xi = \sqrt{\frac{\Phi_0}{2\pi B_{c2}}}$ is approximately 55 nm at optimal doping, where Φ_0 is the flux quantum, and increases to hundreds of nm when $\tilde{n}$ approaches half-filling or the von Hove singularity (Fig. 2e, right axis). These values of T_c, B_{c2} and ξ are similar to those in prior reports[4,6,20,27,28].

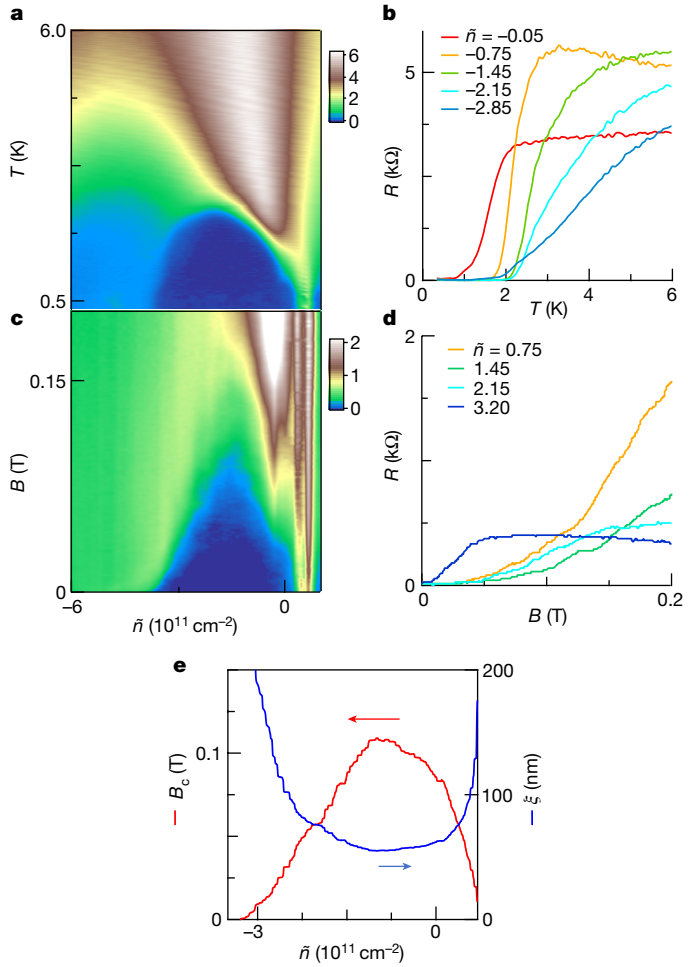

Fig. 2 | Zero-bias transport data at $B = 0$. a–b, $R(T, \tilde{n})$ in kΩ showing the superconducting dome (dark blue), and line traces $R(T)$ at different $\tilde{n}$ (in 10^{11} cm^{-2}). **c–d**, $R(B, \tilde{n})$ at $T = 0.3$ K, and line traces at different $\tilde{n}$. **e**, Critical magnetic field B_c and superconducting coherence length ξ versus $\tilde{n}$.

From these ξ and velocity measurements, several fundamental BCS relations are clearly invalidated. For example, the pairing gap is given by $\Delta \approx \hbar v_F/\xi$. Using $v_n \approx v_F \approx 1{,}000$ m s^{-1} as a characteristic velocity and $\xi = 55$ nm at optimal doping, $\Delta/k_B T_c$ is found to be around 0.05, far smaller than the ratio of 1.75 in conventional superconductors. Similarly, Pippard's argument using the uncertainty principle to obtain $\xi \approx \Delta x \approx \frac{\hbar v_F}{k_B T_c}$, yields $\xi \approx 2.6$ nm at optimal doping, much smaller than that measured from B_{c2} data, or the expected lower bound given by the characteristic interparticle spacing. Another fundamental quantity is the superfluid stiffness D_s that determines the superconductor's electromagnetic response. Conventionally, $D_s(T) = e^2 n_s(T)/m^*$, where n_s is the superfluid density and m^* is the effective mass of carriers. Using the simple approximation $m^* = \hbar k_F/v_n$, where $k_F = \sqrt{2\pi\tilde{n}}$ is the Fermi wave vector (the factor of 2 arises from the twofold quasiparticle degeneracy near $\nu = -1/2$ (refs.[3,6,20,21])), and assuming $n_s(0) = \tilde{n}$, we find $D_s(0) \approx 10^6$ H^{-1} at optimal doping. Since D_s yields an upper bound of Berezinskii–Kosterlitz–Thouless transition through the Nelson–Kosterlitz criterion[29]

$$\frac{\hbar^2 D_s(0)}{e^2 k_B T_c} \geq \frac{8}{\pi} \tag{1}$$

our estimated $D_s(0)$ thus yields $T_c \leq 0.05$ K at optimal doping, far below the observed $T_c = 2.2$ K. We emphasize that the arguments presented above are based on order-magnitude estimates, and will not be affected even if v_n is reduced from v_F by a factor of 2, whereas our calculations show that v_n and v_F agree within 30% over the relevant density range (Extended Data Fig. 5). Therefore, all these invalidated equations indicate that the flat band superconductivity is markedly different from the conventional (BCS-like) behaviour.

Superconducting state: critical current

We now focus on non-linear transport in the superconducting state. Figure 3a plots dV/dI versus J and $\tilde{n}$. For $|\tilde{n}| > 4.0 \times 10^{11}$ cm^{-2}, the dV/dI peaks are identical to those at $B = 0.2$ T (Fig. 3b). In the superconducting state, the same 'bell-like' features persist, with almost identical outlines of critical current density as in Fig. 1b. However, two important features differ in the superconducting and normal states. First, throughout the underdoped region, the high-bias peaks are extremely sharp, and they are suppressed at a small B. We therefore identify these very sharp peaks as corresponding to the superconducting critical current density J_{cs}. Surprisingly and importantly, $J_{cs} \approx J_{cn}$ for this underdoped region—that is, the peak positions are almost identical in both the superconducting and normal states (Fig. 3c,d). Second, at higher doping ($\tilde{n} < -2.0 \times 10^{11}$ cm^{-2}), the dV/dI peak bifurcates—the outer peak has a similar location and amplitude as that in the normal state; the inner peak occurs at smaller current density and disappears at a small B, thus its location is identified as J_{cs} (Fig. 3e). J_{cs} decreases rapidly with increasing doping in this overdoped region, vanishing at $\tilde{n} \approx -3.8 \times 10^{11}$ cm^{-2}.

Figure 3f plots J_{cs} and J_{cn} as red circles and blue circles, respectively. The bifurcation of J_{cn} and J_{cs} in the overdoped regime suggests that two distinct mechanisms limit the superconducting critical current, while their coincidence in the underdoped regime indicates that the supercurrent is regulated by the same current-limiting mechanism in the normal state, namely the band velocity limit in a Dirac system.

Conventionally, J_{cs} is limited by the depairing condition[30]—a supercurrent with uniform velocity v_s shifts the energy of quasiparticle excitations by $\hbar k_F v_s$, and superconductivity is destroyed when this energy shift exceeds Δ, yielding

$$J_{cs} = n_s e \frac{\Delta}{\hbar k_F} = n_s e \frac{\alpha k_B T_c}{\hbar k_F} \tag{2}$$

where $n_s \approx \tilde{n}$ at low temperatures, and $\Delta = \alpha k_B T_c$. Assuming $\alpha \approx 2$ across the entire doping range, based on prior parallel field and scanning tunnelling spectroscopy studies[4,31,32], we find that the depairing critical current obtained from equation (2) (Fig. 3f, dotted black curve) is at least an order of magnitude higher than the measured J_{cs}.

Now we consider the new limiting mechanism to the supercurrent—that is, the vanishingly small band velocity. The depairing condition in a conventional superconductor implicitly assumes that (1) the energy shift $\hbar k_F v_s$ represents a small perturbation of the Fermi sea, and (2) the band dispersion is quadratic, so that there is no saturation limit to v_s (Fig. 3g). However, neither of these assumptions applies in tBLG with flat Dirac minibands. In a gapless Dirac spectrum, while the condensate's momentum and velocity are proportional at small momentum, the velocity saturates to the band velocity v_F at large momentum, as illustrated in Fig. 3h–j. As J increases from zero, the order parameter phase gradient $\nabla\varphi$ continuously grows, while v_s asymptotically approaches v_F. This is analogous to the acceleration of a particle in special relativity, where the relativistic mass continuously increases while its speed asymptotically approaches the speed of light. Once $\nabla\varphi \approx 1/\xi$, superconductivity is destroyed, and $v_s \approx v_F$. Larger currents are then enabled via the Schwinger mechanism.

In the underdoped regime, as $k_F \propto \sqrt{\tilde{n}}$ is very small, such velocity saturation is expected to occur before the depairing limit; in the overdoped regime, however, Δ diminishes while k_F increases, and the depairing condition equation (2) becomes limiting. A full theoretical treatment of J_{cs} is beyond the scope of the work. Nevertheless, as it is determined

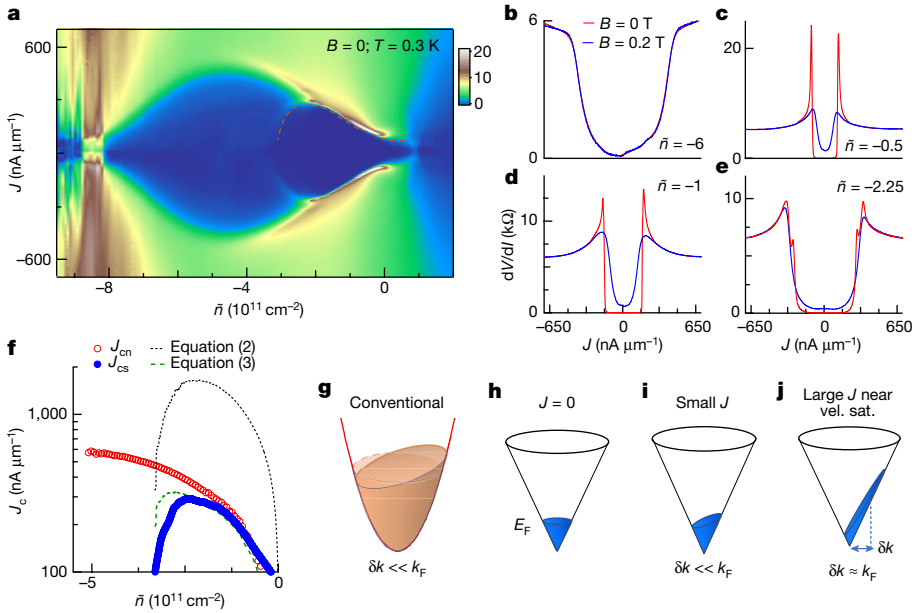

Fig. 3 | Nonlinear transport data in the superconducting regime. a, dV/dI (J, $\tilde{n}$) in kΩ. The dotted line outlines the superconducting region for $J > 0$. **b**–**e**, dV/dI (J) at $B = 0$ and $B = 0.2$ T, and different densities ($\tilde{n}$ labelled in units of 10^{11} cm^{-2}), respectively. **f**, Extracted critical current density in superconducting (blue) and normal (red circles) states. The black dotted line is calculated using the depairing condition equation (2), and green dotted line using equation (3) by taking both depairing and velocity saturation into account. **g**, Schematic of Fermi energy shift in a conventional superconductor with a quadratic dispersion and $\Delta << E_F$. **h**–**j**, Schematics of Fermi energy in a Dirac band with small v_F in the limits of $J = 0$, small J and large J near velocity saturation, respectively. Here δk is the change in the average momentum of the charge carriers between zero and finite J. In **g**–**i** charges condense below the superconducting gap Δ. For simplicity of illustration, Δ and thermal smearing of the charge distribution are not shown.

by the smaller of these two limits, we phenomenologically write the effective velocity as

$$v^{-1} = v_n^{-1} + \left(\frac{\Delta}{\hbar k_F}\right)^{-1} \quad (3)$$

and calculate $J_{cs} = \tilde{n}ev$. The green dashed line in Fig. 3f shows the resulting curve, in reasonable agreement with the experimental data, thus confirming the presence of both conventional and unconventional limits to supercurrent density in magic angle tBLG.

Quantum geometry and superfluid stiffness

The observed J_{cs} also enables an estimation of D_s in this flat band superconductor. Since conventional techniques of measuring D_s cannot be applied to mesoscopic devices, we extract D_s from our data by relating D_s and the gauge invariant momentum, $\mathbf{p} = \hbar\nabla\varphi - 2e\mathbf{A}$, to the supercurrent $\mathbf{J} = \frac{D_s}{2e}\mathbf{p}$, where φ is the phase of the superconducting order parameter and $\mathbf{A}$ is the vector potential. The vortex core radius, which is characteristically ξ, is determined by the condition where the circulating current density reaches its critical value J_c[33] (Fig. 4a inset). Using $|\nabla\varphi| \approx 1/\xi$, we obtain

$$D_s(0) = \frac{2\pi J_{cs}\xi}{\Phi_0} \quad (4)$$

where $\Phi_0 = h/2e$ is the flux quantum. The extracted $D_s(0)$ using experimentally measured J_{cs} and ξ follows a dome-like behaviour with a maximum of about 5×10^7 H^{-1} (solid red line in Fig. 4a), far larger than the conventional estimate (black dotted line), while also exhibiting a maximum, where the conventional estimate is monotonic in density. Putting this value into equation (1) yields $T_c \approx 0.6$ K without free parameters. Though lower than the measured $T_c = 2.2$ K at optimal doping, its agreement within the same order of magnitude is reasonable, particularly considering the model's simplicity.

To understand the measured D_s we turn to recent insights from mean field theories[8–13] and exact bounds[12,34] for D_s in flat band systems. Here the conventional D_s contribution from band dispersion is absent, consistent with the small experimental estimate presented above. Instead, the diamagnetic response is determined by the wavefunctions' quantum geometry through the trace of the quantum metric or the non-trivial band topology for tBLG[35–39]. The scale of D_s is set not by the kinetic energy but by the interactions, thus it scales with Δ[8–12,40]. Absent a theory for the full density dependence of superconductivity in tBLG that includes resets at

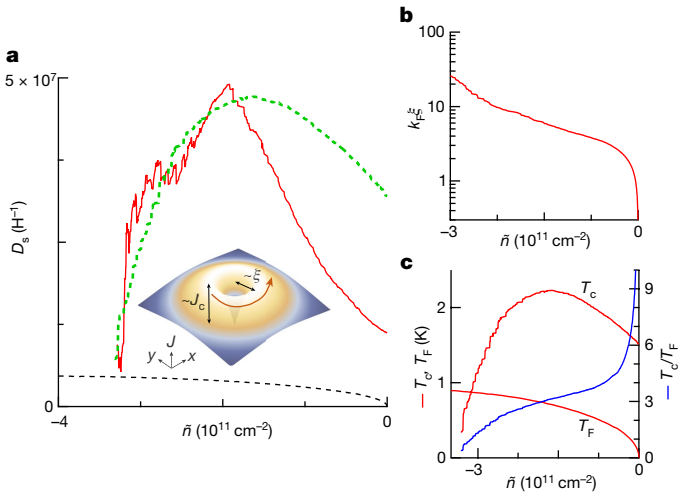

Fig. 4 | Superfluid stiffness and characteristic temperatures of the flat band. a, Inset, supercurrent density circulating around a vortex core with radius $r \approx \xi$. $J \sim 1/r$ ($J \sim r$) at large $r >> \xi$ (at small $r << \xi$,), with a peak J_c at $r = \xi$. Main panel, superfluid stiffness D_s versus $\tilde{n}$. The red line is calculated from equation (4) using experimentally measured J_c and ξ. The black dotted line is calculated using the conventional expression $D_s(T) = e^2 n_s(T)/m^*$, and the green dotted line using $D_s(0, \tilde{n}) \approx b\frac{e^2}{\hbar^2}\Delta(0, \tilde{n})$ with $b = 0.33$. **b**, $k_F\xi$ versus $\tilde{n}$ at $T = 0.3$ K. **c**, T_c and T_F (right axis) and their ratio (left axis) versus $\tilde{n}$.

half-filling, we use dimensional analysis to estimate $D_s(0,\tilde{n}) \approx b\frac{e^2}{\hbar^2}\Delta(0,\tilde{n})$, where b is a constant of order unity. Using $\Delta(0,\tilde{n}) \approx 2k_B T_c(\tilde{n})$ and $b = 0.33$, we obtain the green dotted curve in Fig. 4a, which has the same general dome-shaped curve as that extracted experimentally. This qualitative agreement thus provides strong evidence that D_s in tBLG is dominated by the interaction-driven quantum geometric contribution, rather than the conventional contribution with a scale set by band dispersion.

Strong-coupling superconductivity

Superconductivity in an ultra-flat band system, where interactions are comparable to or exceed the bandwidth, is expected to be very strongly coupled. Examining the ratio of pair size, estimated by comparing the coherence length ξ to the interparticle distance $1/k_F$ (Fig. 4b), we find very small values of $k_F\xi$ that between 1 (underdoped) to 10 (overdoped), characteristic of the strong coupling regime of the BCS to Bose–Einstein condensation crossover[17–19]. This is also consistent with recent observations of a pseudogap in scanning tunnelling microscopy studies of tBLG[31,41].

We next plot T_c, the Fermi temperature T_F and their ratio versus $\tilde{n}$ in Fig. 4c, where $T_F = \hbar v_n k_F/k_B$. Remarkably, T_c/T_F exceeds 1 for almost the entire dome; in the underdoped regime $T_c/T_F >> 1$. The large T_c/T_F arises from the very small density $\tilde{n}$, due to the reset at half-filling, combined with the extremely small v_n, so that $T_F \approx 0.24$ K even at optimal doping. Such large values of T_c/T_F are unprecedented and different from all other superconductors in the Uemura plot[4,42] of T_c versus T_F. Note that this T_F is not the 'bare' value related to the total density in the eight low-energy bands of tBLG, but already renormalized by the interactions that lead to the reset.

To explain this large T_c/T_F ratio, we note that $T_c \leq T_F/8$ only for parabolic dispersion[34], while the general bound on T_c is in terms of the optical sum rule. In a gapless Dirac system, there is finite optical spectral weight from interband transitions in the limit of E_F coinciding with the Dirac nodes, thus the T_c is not limited by T_F. Moreover, T_F is vanishingly small for any flat band superconductor (Dirac or otherwise), but in a superconducting Dirac system the quantum geometric contributions to the low-energy optical spectral weight and D_s are finite[12,34], leading to a finite T_c. We thus understand why tBLG, a flat band Dirac system, is in an unprecedented regime with $T_c/T_F > 1$.

In conclusion, tBLG requires us to face the challenge of ultra-strong coupling superconductivity in flat band Dirac systems, where, naively, there can be no transport or superconductivity. This work provides experimental evidence that the superfluid stiffness in ultra-flat band tBLG is dominated by quantum geometric contributions, calls for a deeper understanding of how superconductivity arises in flat bands with non-trivial topology[38,39], and how well-known BCS relations are modified when quantum geometric effects dominate, and points to a possible new guiding principle for the search for high-T_c superconductors.

Online content

Any methods, additional references, Nature Portfolio reporting summaries, source data, extended data, supplementary information, acknowledgements, peer review information, details of author contributions and competing interests, and statements of data and code availability are available at https://doi.org/10.1038/s41586-022-05576-2.

1. Lee, P. A., Nagaosa, N. & Wen, X.-G. Doping a Mott insulator: physics of high-temperature superconductivity. *Rev. Mod. Phys.* **78**, 17 (2006).
2. Stewart, G. R. Unconventional superconductivity. *Adv. Phys.* **66**, 75–196 (2017).
3. Cao, Y. et al. Correlated insulator behaviour at half-filling in magic-angle graphene superlattices. *Nature* **556**, 80 (2018).
4. Cao, Y. et al. Unconventional superconductivity in magic-angle graphene superlattices. *Nature* **556**, 43 (2018).
5. Andrei, E. Y. & MacDonald, A. H. Graphene bilayers with a twist. *Nat. Mater.* **19**, 1265–1275 (2020).
6. Balents, L., Dean, C. R., Efetov, D. K. & Young, A. F. Superconductivity and strong correlations in moiré flat bands. *Nat. Phys.* **16**, 725–733 (2020).
7. Lau, C. N., Bockrath, M. W., Mak, K. F. & Zhang, F. Reproducibility in the fabrication and physics of moiré materials. *Nature* **602**, 41–50 (2022).
8. Peotta, S. & Törmä, P. Superfluidity in topologically nontrivial flat bands. *Nat. Commun.* **6**, 8944 (2015).
9. Hu, X., Hyart, T., Pikulin, D. I. & Rossi, E. Geometric and conventional contribution to the superfluid weight in twisted bilayer graphene. *Phys. Rev. Lett.* **123**, 237002 (2019).
10. Xie, F., Song, Z., Lian, B. & Bernevig, B. A. Topology-bounded superfluid weight in twisted bilayer graphene. *Phys. Rev. Lett.* **124**, 167002 (2020).
11. Julku, A., Peltonen, T. J., Liang, L., Heikkilä, T. T. & Törmä, P. Superfluid weight and Berezinskii-Kosterlitz-Thouless transition temperature of twisted bilayer graphene. *Phys. Rev. B* **101**, 060505 (2020).
12. Verma, N., Hazra, T. & Randeria, M. Optical spectral weight, phase stiffness, and Tc bounds for trivial and topological flat band superconductors. *Proc. Nat. Acad. Sci.* **118**, e2106744118 (2021).
13. Herzog-Arbeitman, J., Peri, V., Schindler, F., Huber, S. D. & Bernevig, B. A. Superfluid weight bounds from symmetry and quantum geometry in flat band. Phys. Rev. Lett. **128**, 087002 (2022)
14. Berdyugin, A. I. et al. Out-of-equilibrium criticalities in graphene superlattices. *Science* **375**, 430–433 (2022).
15. Schwinger, J. On gauge invariance and vacuum polarization. *Phys. Rev.* **82**, 664–679 (1951).
16. Nishida, Y. & Abuki, H. BCS-BEC crossover in a relativistic superfluid and its significance to quark matter. *Phys. Rev. D* **72**, 096004 (2005).
17. Chen, Q., Stajic, J., Tan, S. & Levin, K. BCS–BEC crossover: from high temperature superconductors to ultracold superfluids. *Phys. Rep.* **412**, 1–88 (2005).
18. Randeria, M. & Taylor, E. Crossover from Bardeen-Cooper-Schrieffer to Bose-Einstein Condensation and the Unitary Fermi Gas. *Annu. Rev. Condens. Matter Phys.* **5**, 209–232 (2014).
19. Nakagawa, Y. et al. Gate-controlled BCS-BEC crossover in a two-dimensional superconductor. *Science* **372**, 190–195 (2021).
20. Lu, X. et al. Superconductors, orbital magnets, and correlated states in magic angle bilayer graphene. *Nature* **574**, 653 (2019).
21. Zondiner, U. et al. Cascade of phase transitions and Dirac revivals in magic-angle graphene. *Nature* **582**, 203–208 (2020).
22. Allor, D., Cohen, T. D. & McGady, D. A. Schwinger mechanism and graphene. *Phys. Rev. D* **78**, 096009 (2008).
23. Polshyn, H. et al. Large linear-in-temperature resistivity in twisted bilayer graphene. *Nat. Phys.* **15**, 1011–1016 (2019).
24. Park, J. M., Cao, Y., Watanabe, K., Taniguchi, T. & Jarillo-Herrero, P. Flavour Hund's coupling, Chern gaps and charge diffusivity in moiré graphene. *Nature* **592**, 43–48 (2021).
25. Berezinsky, V. L. Destruction of long range order in one-dimensional and two-dimensional systems having a continuous symmetry group. I. Classical systems. *Sov. Phys. JETP* **32**, 493–500 (1971).
26. Kosterlitz, J. M. & Thouless, D. J. Ordering, metastability and phase transitions in two-dimensional systems. *J. Phys. C: Solid State Phys.* **6**, 1181–1203 (1973).
27. Yankowitz, M. et al. Tuning superconductivity in twisted bilayer graphene. *Science* **363**, 1059 (2019).
28. Codecido, E. et al. Correlated insulating and superconducting states in twisted bilayer graphene below the magic angle. *Sci. Adv.* **5**, eaaw9770 (2019).
29. Nelson, D. R. & Kosterlitz, J. M. Universal jump in the superfluid density of two-dimensional superfluids. *Phys. Rev. Lett.* **39**, 1201 (1977).
30. Tinkham, M. *Introduction to Superconductivity* 2nd edn (McGraw-Hill, 1996).
31. Oh, M. et al. Evidence for unconventional superconductivity in twisted bilayer graphene. *Nature* **600**, 240–245 (2021).
32. Cao, Y. et al. Nematicity and competing orders in superconducting magic-angle graphene. *Science* **372**, 264–271 (2021).
33. Sensarma, R., Randeria, M. & Ho, T.-L. Vortices in superfluid Fermi gases through the BEC to BCS crossover. *Phys. Rev. Lett.* **96**, 090403 (2006).
34. Hazra, T., Verma, N. & Randeria, M. Bounds on the superconducting transition temperature: applications to twisted bilayer graphene and cold atoms. *Phys. Rev. X* **9**, 031049 (2019).
35. Ahn, J., Park, S. & Yang, B.-J. Failure of Nielsen-Ninomiya theorem and fragile topology in two-dimensional systems with space-time inversion symmetry: application to twisted bilayer graphene at magic angle. *Phys. Rev. X* **9**, 021013 (2019).
36. Po, H. C., Zou, L., Senthil, T. & Vishwanath, A. Faithful tight-binding models and fragile topology of magic-angle bilayer graphene. *Phys. Rev. B* **99**, 195455 (2019).
37. Song, Z. et al. All magic angles in twisted bilayer graphene are topological. *Phys. Rev. Lett.* **123**, 036401 (2019).
38. Ma, C. et al. Moiré band topology in twisted bilayer graphene. *Nano Lett.* **20**, 6076–6083 (2020).
39. Fortin-Deschênes, M. et al. Uncovering Topological Edge States in Twisted Bilayer Graphene. *Nano Lett.* **22**, 6186–6193 (2022).
40. Khalaf, E., Chatterjee, S., Bultinck, N., Zaletel, M. P. & Vishwanath, A. Charged skyrmions and topological origin of superconductivity in magic-angle graphene. *Sci. Adv.* **7**, eabf5299 (2021).
41. Jiang, Y. et al. Charge order and broken rotational symmetry in magic-angle twisted bilayer graphene. *Nature* **573**, 91–95 (2019).
42. Uemura, Y. J. et al. Basic similarities among cuprate, bismuthate, organic, Chevrel-phase, and heavy-fermion superconductors shown by penetration-depth measurements. *Phys. Rev. Lett.* **68**, 2712–2712 (1992).

Methods

Device fabrication and measurements

Before the stacking process, a selected monolayer graphene flake is cut with the tip of an atomic force microscope to minimize the introduction of strain originating from flake tearing[43]. A poly(bisphenol A carbonate)/polydimethylsiloxane stamp mounted on a glass slide is used to pick up, sequentially, the top BN, the first-layer graphene, the second-layer graphene after a rotation of approximately 1.1–1.2 degrees and the bottom BN. The entire stack is deposited onto an SiO_2 (300 nm)/Si chip. A bubble-free region is selected, and the device geometry is defined by electron beam lithography and etching with CHF_3/O_2 plasma. The tBLG device is coupled to contacts by depositing Cr/Au (10 nm/90 nm) metal electrodes.

The devices are measured in an He^3 refrigerator or flowing He gas cryostat using standard lock-in techniques. The a.c. excitation current is 5 nA at 17 Hz, with a time constant of 300 ms.

Landau fan over extended range

Extended Data Fig. 1 displays longitudinal resistance R_{xx} over large ranges of V_{bg} and B at $T = 0.3$ K. It displays several characteristics that are in agreement with earlier works—peaks at $\nu = 0, -1/4, \pm1/2, -3/4$ and ±1, and one-sided Landau fans. We note that the peak at $\nu = -1/4$, which has been previously attributed to an isospin Pomeranchuck effect, onsets at a lower magnetic field than prior works[44,45], suggesting a smaller spin stiffness. This may arise from the very narrow bandwidth and stronger electronic interactions in our device, which favours spontaneous spin polarization, consistent with the Stoner criterion. However, more work will be required to fully understand the origin of this behaviour.

In addition to the peaks at quarter- and half-filling, the device also displays a number of peaks at other fractions. Using the convention that the full-filling of the minibands correspond to filling factor $\tilde{\nu} = \pm4$, we identify a number of peaks at fractional fillings of $\tilde{\nu} = -0.5$, 1.5 and $N \pm 1/3$, where N is an integer. Similar peaks are observed in a recent work from Massachusettes Institute of Technology and Harvard groups[46], and are attributed to charge density wave and Chern insulator states arising from quantum geometry. Also, the presence of fractional correlated insulating states at $N \pm 1/3$ filling factors in magic angle tBLG have been predicted by a recent work[47].

Band structure calculation of tBLG

The moiré band structure of tBLG with a small twist angle is obtained by using the 2011 Bistritzer–MacDonald model[48]. In the original model, the AA and AB interlayer tunnelling amplitudes are $t_{AA} = t_{AB} = 110$ meV, and the Fermi velocity is $v_F = 1 \times 10^6$ m s^{-1}. The refined parameter values[49] $t_{AA} = 79.7$ meV, $t_{AB} = 97.5$ meV and $v_F = 7.98 \times 10^5$ m s^{-1} were used here to take into account the corrugation effect due to lattice relaxation and to better match the previous experimental observations. In our model, the momentum cutoff is six times the moiré reciprocal lattice vectors. Namely, the considered momentum-space area, centred at the K point in the original Brillouin zone, is 108 times the area of the first moiré Brillouin zone. Each moiré band is spin degenerate, since the spin-orbit coupling is negligibly weak in tBLG. The moiré bands at valley K′ of the original Brillouin zone (not shown) can be obtained by using the time reversal symmetry.

Relating drift velocity and Fermi velocity

Consider a reference frame moving at the drift velocity v_n in the x direction. The Galilean transformation ($v_F \ll c$) of space–time coordinates and energy of a massless particle reads as follows: $t' = t$, $E' = E - v_n p_x$, $y' = y$ and $E' = E - v_n p_x$ (Fig. 3h,i). By assuming that in the moving frame electrons have stationary Fermi distribution[14]—that is, at zero temperature every state below the Fermi energy E'_F is filled—the Fermi surface in the lab frame is thus determined by $E'_F = v_F\sqrt{p_x^2 + p_y^2} - v_n p_x$, where p_x and p_y are the x and y components of momentum $\boldsymbol{p}$. It follows that the Fermi surface in the lab frame is an ellipse described by $(p_x - p_{x0})^2/a^2 + p_y^2/b^2 = 1$, where $p_{x0} = v_n E'_F/(v_F^2 - v_n^2)$ is the ellipse centre, $a = \gamma^2 E'_F/v_F$ and $b = \gamma E'_F/v_F$ are respectively the semi-major and semi-minor axes, $\beta = v_n/v_F$ and $\gamma = 1/\sqrt{1-\beta^2}$ (Fig. 3i). The area of the ellipse measures the density of electrons in the conduction band: $n_e = \int_{\text{ellipse}} (d^2p)/h^2$. These yield the relation $E'^2_F = n_e h^2 v_F^2/(\pi\gamma^3)$. As v_n increases, the momentum-space distribution of electrons is squeezed along the velocity direction in the lab frame. When $v_n = v_F$, the ellipse crosses the Dirac point, and all the electrons in the conduction band (if n-doped) are pushed to one side of the Dirac cone. (The p-doped case is similar). To increase the current further, it must involve excitations coming from the valence band—that is, the Schwinger mechanism needs to be triggered. Inserting E'_F back to a and b reveals the geometric deformation of the Fermi surface: $a \propto \gamma^{1/2}$ and $b \propto \gamma^{-1/2}$, leaving the area and thus the density invariant. The ellipse is elongated and becomes a line (eccentricity goes from 1 to 0) when $v_n = v_F$ (Fig. 3j and Extended Data Fig. 4). In this limit, all the electrons have $p_y = 0$ in the lab frame.

Further consider the realistic case in which the Fermi velocity v_F decreases as the Fermi energy increases from the Dirac point (where the crossing bands are perfectly linear) to the van Hove singularity (where the two Dirac cones meet). In this case, the critical drift velocity v_n ($v_n = v_F$ in the ideal case above) is a function of the Fermi energy, or in other words, the carrier density. Without loss of generality, we model the non-linear energy-momentum dispersion by using $E = E_0 \tanh(v_{DP}\sqrt{p_x^2 + p_y^2}/E_0)$, where v_{DP} is the Fermi velocity at the Dirac point, and E_0 is a saturation energy at the van Hove singularity. Following our band structure calculations, we choose $v_{DP} = 1{,}000$ m s^{-1} and $E_0 = 0.5$ meV. A similar analysis shows that, as the electron density n_e goes up, the Fermi velocity v_F decreases, the effective mass at Fermi energy $m^* = \hbar k_F/v_F$ increases and the corresponding critical drift velocity v_n decreases. These results are summarized in Extended Data Fig. 5. Importantly, both v_F and v_n are still in the same order of magnitude as v_{DP}. In fact, the ratio v_n/v_F is close to 1 for small densities and larger than 0.6 for the largest reduced density (defined from the resettled Dirac point at integer electron/hole fillings) relevant to our experiments.

Schwinger mechanism

In high-energy physics, the Schwinger mechanism[15] describes how the vacuum decays owing to a large electric field that breaks down the gap between electrons and positrons. In condensed matter physics, the massless feature of graphene is favourable for the realization of the Schwinger mechanism[15,22,50]. Moreover, the chemical potential can be tuned above/below the Dirac point by charge doping, and a critical current is thus needed to deplete the carriers for the electron–hole pair creation to occur. In tBLG near the magic angle, the Fermi velocity can be about 10^{-3} times smaller than that of monolayer graphene, making the Schwinger mechanism easier to observe. However, interaction may induce a mean-field gap m at the Dirac point, which needs to be overcome. To assess these effects, we introduce the rate for electron–hole creation induced by an electric field $\mathbf{E}$ (ref. [22])

$$\Gamma = \frac{(qE)^{3/2}}{\pi^2\hbar^{3/2}v_F^{1/2}}\exp\left(-\frac{\pi m^2 v_F^3}{qE\hbar}\right),$$

where q is the electron charge and v_F is the Fermi velocity. For a finite sample of length L and width W, it leads to the following current density:

$$j = \frac{I}{W} = \frac{q\Gamma LW}{W} = \frac{q(qV)^{3/2}}{\pi^2\hbar^{3/2}v_F^{1/2}L^{1/2}}\exp\left(-\frac{\pi m^2 v_F^3 L}{qV\hbar}\right).$$

Moreover, the differential conductivity reads:

$$\frac{\mathrm{d}j}{\mathrm{d}V} = \frac{q}{\pi^2\hbar^{3/2}v_\mathrm{F}^{1/2}L^{1/2}}\left(\frac{3}{2}q^{3/2}V^{1/2} + \frac{\pi m^2 v_\mathrm{F}^3 L q^{1/2}}{V^{1/2}\hbar}\right)\exp\left(-\frac{\pi m^2 v_\mathrm{F}^3 L}{qV\hbar}\right)$$
$$= \frac{j}{(qV)^{3/2}}\left(\frac{3}{2}q^{3/2}V^{1/2} + \frac{\pi m^2 v_\mathrm{F}^3 L q^{1/2}}{V^{1/2}\hbar}\right).$$

For $m = 0$, this yields an I–V curve with $I \propto V^{3/2}$ and a differential conductivity map with $\mathrm{d}j/\mathrm{d}V \propto j^{1/3}$.

Fermi velocity determined by non-linear transport measurements and other methods

To compare the band velocity measurements obtained from non-linear transport (v_NLT) to those obtained from measuring the quantum Hall gap at filling factor 4 (v_QH), we first measure v_NLT near charge neutrality from the slope of the Schwinger peak features, as shown in Extended Data Fig. 6a for device D2. This is similar to the method discussed in the main text. This yields $v_\mathrm{NLT} = 3.6 \times 10^4\ \mathrm{m\ s^{-1}}$. We then measure the temperature dependence of R_{xx} in the filling factor $\nu_q = 4$ quantum Hall state (Extended Data Fig. 6b). An activation plot of R_{xx} in the $\nu_q = 4$ resistance minimum at density $n_\mathrm{min} \approx 0.4 \times 10^{12}\ \mathrm{cm^{-2}}$ is shown in the inset. This yields an energy gap of around 2.1 meV for D2. The velocity is estimated from the nth Landau level energies for a Dirac spectrum, $E_\mathrm{n} = v_\mathrm{F}\sqrt{2e\hbar Bn}$, yielding $v_\mathrm{QH} = 2.9 \times 10^4\ \mathrm{m\ s^{-1}}$ for D2.

A similar analysis yields $v_\mathrm{NLT} = 2.7 \times 10^4\ \mathrm{m\ s^{-1}}$ and $v_\mathrm{QH} = 1.1 \times 10^4\ \mathrm{m\ s^{-1}}$ for device D3 (Extended Data Fig. 6c,d). Note that while Extended Data Fig. 6c shows mainly a dominant upward sloping feature, a negative sloping feature with a slope of similar magnitude is present (see inset), though not prominent with respect to the background. Nevertheless, despite the lower-quality data from this device, the measured velocity is consistent with the other data points obtained by the various methods shown in Fig. 1e. Moreover, the agreement of slope magnitudes between the upward and downward sloping features in Extended Data Figs. 6a,c and 7 indicate that the contact resistance is not large enough to cause gate shift artefacts in the devices arising from the voltage bias. The extracted values of v_QH are plotted against v_NLT for D2 and D3 in Extended Data Fig. 6e. The red dashed line corresponds to $v_\mathrm{NLT} = v_\mathrm{QH}$, showing the agreement between the two methods of velocity measurement.

Figure 1e shows that velocities near the charge neutrality obtained using the Schwinger mechanism are consistent with previous literature. On the other hand, we note that the velocity measured near charge neutrality is typically significantly larger than that measured near half-filling. An example is shown for device D4 in Extended Data Fig. 7. The velocity obtained near charge neutrality of $1.7 \times 10^4\ \mathrm{m\ s^{-1}}$ is nearly an order of magnitude larger than that obtained near half-filling ($2.3 \times 10^3\ \mathrm{m\ s^{-1}}$). This is consistent with previous studies that also show that compared to charge neutrality, at half-filling a larger mass[3,4] and a lower velocity[14] are observed.

'Residual' resistance

The superconducting region in Figs. 2 and 3 has an apparent resistance of about 20–30 Ω, as shown in the left panel in Extended Data Fig. 8a. This, however, should not be taken as the true resistance value of the superconducting state as these data are taken with a.c. lock-in measurements optimized for a large dynamic range (up to around 50 kΩ), and the 20–30 Ω arises from an instrumental offset. A more accurate measurement of the resistance in the superconducting state can be achieved by acquiring slow-sweep d.c. voltage–current characteristics. An example is shown for such a curve at $\tilde{n} = -1.65 \times 10^{11}\ \mathrm{cm^{-2}}$, which displays an exceedingly flat segment for $J < J_\mathrm{cs}$; fitting a straight line to the segment around zero bias yields a slope of $-0.2 \pm 1.4\ \Omega$, indicating a zero resistance state within the measurement noise (Extended Data Fig. 8b).

Non-linear transport at other filling fractions

Extended Data Figure 9 plots non-linear measurements of $\mathrm{d}V/\mathrm{d}I$ versus current density J and filling fraction ν over the entire range of full band filling. Peaks in $\mathrm{d}V/\mathrm{d}I$ are observed for filling fractions between 1/2 and 5/8 filling of the moiré superlattice on both hole-doped and electron-doped regimes, though the data are not entirely electron–hole symmetric. For $\nu > 1/2$, it appears that the band's group velocity is higher than that of the valence band; however, the device characteristics are too unstable over the said density range for definitive conclusions to be drawn.

Role of disorder and twist angle domains

The twist angle is determined from the density values of the half-filling and full-filling peaks, and the charge density is determined from the capacitance between the device and the back gate, calculated from the Landau fans and confirmed by geometric considerations. The estimated error bar of twist angle is less than ±0.02°.

Domains with slightly different twist angles are likely to be present in tBLG devices. However, it is unlikely that the transport characteristics of the device are significantly altered by such domains, for the following reasons. First, the observed superconductivity of the device rules out resistive (non-superconducting) regions that are in series over the channel length. Second, the current limit is the same in the normal and superconducting states in the underdoped regime, which, unless the current is distributed over the entire sample width, is extremely unlikely and becoming nearly impossible to occur over an extended density range. Third, theoretically, twist angle domains are not expected to significantly affect transport[51]. Finally, and more fundamentally, the resistance of a conductor is $R \geq h/(N2e^2)$, where N is the number of quantum channels, $N \approx W/\lambda$, where W is the constriction width and λ is the Fermi wavelength; the minimum resistance corresponding to the ballistic limit. From our measured normal state resistance of 500 Ω at a carrier density of $3 \times 10^{15}\ \mathrm{m^{-2}}$, we estimate $W \approx 1\ \mu\mathrm{m}$, which is the sample width. Any scattering would only serve to increase the width estimate; therefore, the agreement of the estimate with the physical width suggests ballistic transport within the Hall bar.

The mean free path l of the device can be estimated using the relation $\sigma / \left(\frac{ge^2}{2h}\right) = k_\mathrm{F} l$, where σ is the two-dimensional resistivity and $g = 2$ is the degeneracy[52]. For $\sigma \approx 560\ \Omega$ (200 Ω) at a carrier density of $1 \times 10^{15}\ \mathrm{m^{-2}}$ ($4 \times 10^{15}\ \mathrm{m^{-2}}$), $l \approx 980$ nm (800 nm), respectively. Considering that the channel length is around 1 μm, these estimates also indicate that the device is in the ballistic regime.

Data availability

The data that support the findings of this study are available from the corresponding authors on reasonable request. Source data are provided with this paper.

Code availability

The code that supports the findings of this study is available from the corresponding authors upon reasonable request.

43. Saito, Y., Ge, J., Watanabe, K., Taniguchi, T. & Young, A. F. Independent superconductors and correlated insulators in twisted bilayer graphene. *Nat. Phys.* **16**, 926–930 (2020).
44. Saito, Y. et al. Isospin Pomeranchuk effect in twisted bilayer graphene. *Nature* **592**, 220–224 (2021).
45. Saito, Y. et al. Hofstadter subband ferromagnetism and symmetry-broken Chern insulators in twisted bilayer graphene. *Nat. Phys.* **17**, 478–481 (2021).
46. Xie, Y. et al. Fractional Chern insulators in magic-angle twisted bilayer graphene. *Nature* **600**, 439–443 (2021).

47. Zhang, K., Zhang, Y., Fu, L. & Kim, E.-A. Fractional correlated insulating states at n±1/3 filled magic angle twisted bilayer graphene. *Commun. Phys.* **5**, 250 (2022)
48. Bistritzer, R. & MacDonald, A. H. Moiré bands in twisted double-layer graphene. *Proc. Nat. Acad. Sci.* **108**, 12233 (2011).
49. Koshino, M. et al. Maximally localized Wannier orbitals and the extended Hubbard model for twisted bilayer graphene. *Phys. Rev. X* **8**, 031087 (2018).
50. Dóra, B. & Moessner, R. Nonlinear electric transport in graphene: quantum quench dynamics and the Schwinger mechanism. *Phys. Rev. B* **81**, 165431 (2010).
51. Sainz-Cruz, H., Cea, T., Pantaleón, P. A. & Guinea, F. High transmission in twisted bilayer graphene with angle disorder. *Phys. Rev. B* **104**, 075144 (2021).
52. Beenakker, C. W. J. & van Houten, H. in *Solid State Physics* Vol. 44 (eds Ehrenreich, H. & Turnbull, D.) 1–228 (Academic Press, 1991).

Acknowledgements We thank P. Stepanov for advice on device fabrication. The experiments are supported by DOE BES Division under grant number DE-SC0020187. M.R. and the nanofabrication facility were supported by NSF Materials Research Science and Engineering Center Grant DMR-2011876. T.X., P.C. and F.Z. were supported by the Army Research Office under grant number W911NF-18-1-0416 and by the National Science Foundation under grant numbers DMR-1945351 through the CAREER programme, DMR-1921581 through the DMREF programme and DMR-2105139 through the CMP programme. T.X., P.C. and F.Z. acknowledge the Texas Advanced Computing Center for providing resources that have contributed to the research results reported in this work. Growth of hexagonal boron nitride crystals was supported by the Elemental Strategy Initiative conducted by the MEXT, Japan (grant number JPMXP0112101001) and JSPS KAKENHI (grant numbers 19H05790, 20H00354 and 21H05233).

Author contributions H.T., C.N.L. and M.W.B. conceived the project. H. T., X.G., Y.Z. and S.C. fabricated samples. H.T. X.G. and Y.Z. performed transport measurements. T.X. and P.C. performed theoretical calculations under the supervision of F.Z. K.W. and T.T. provided hBN crystals. H.T., C.N.L. and M.W.B. analysed the data. M.W.B., C.N.L., M.R. and F.Z. interpreted the data and co-wrote the manuscript. All authors discussed and commented on the manuscript.

Competing interests The authors declare no competing interests.

Additional information

Supplementary information The online version contains supplementary material available at https://doi.org/10.1038/s41586-022-05576-2.

Correspondence and requests for materials should be addressed to Chun Ning Lau or Marc W. Bockrath.

Peer review information *Nature* thanks the anonymous reviewers for their contribution to the peer review of this work.

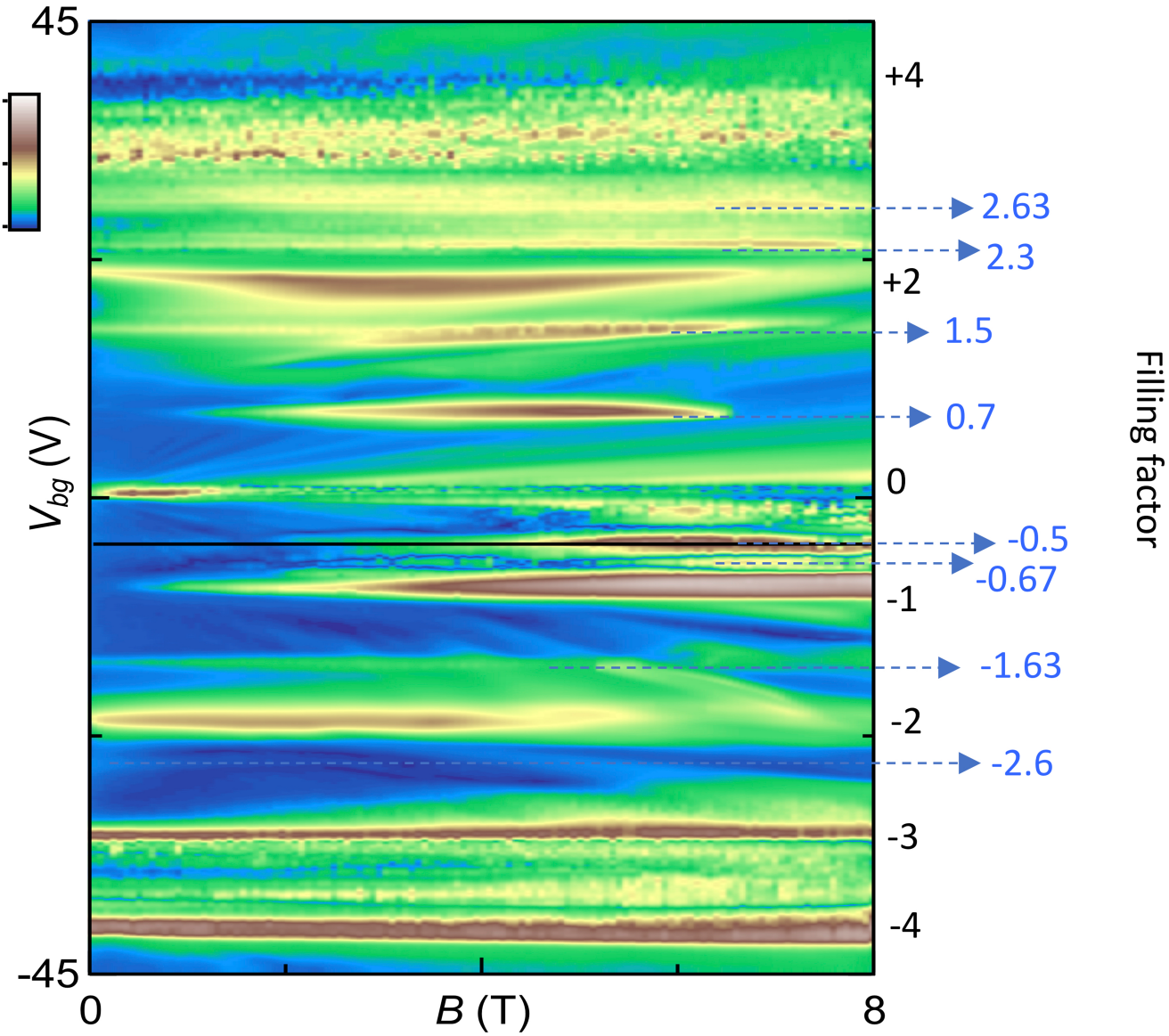

Extended Data Fig. 1 | R_{xx} (V_{bg}, B) of the device at T = 0.3 K. The numbers on the right indicate the filling factors of the peaks (where the full-filling of the minibands correspond to filling factors $\tilde{\nu}$ = ±4). Using the convention that the full-filling of the minibands correspond to filling factor $\tilde{\nu}$ = ±4, we identify a number of peaks at fractional fillings of $\tilde{\nu}$ = −0.5, 1.5 and N ± 1/3, where N is an integer.

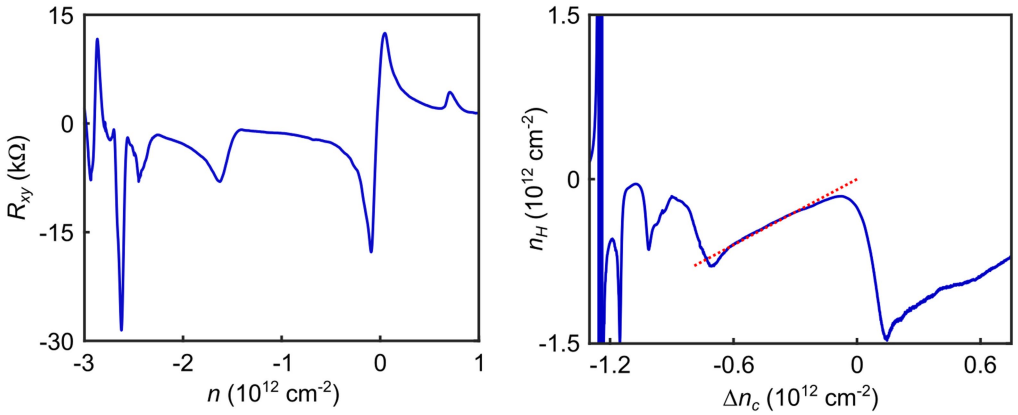

Extended Data Fig. 2 | Hall resistance and inferred charge densities. Left: Symmetrized R_{xy} versus density. Right: Measured Hall density compared to inferred density from capacitance; the red line has a unit slope to show the agreement between the two.

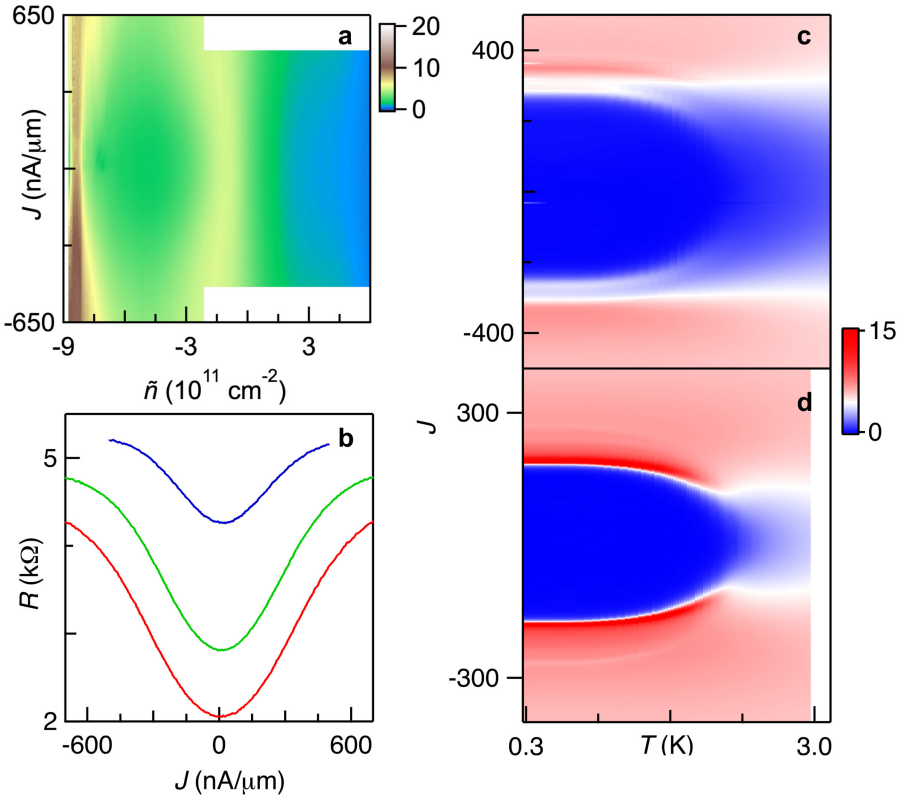

Extended Data Fig. 3 | Non-linear transport at $B = 0$ and higher temperatures. **a**–**b** dV/dI versus J and $\tilde{n}$ at $T = 5$ K, and dV/dI in kΩ versus J at $\tilde{n} = -1$ (blue), −2 (green) and −3 (red) × 10^{11} cm^{-2}, respectively. **c**–**d** dV/dI in kΩ versus J and T at $\tilde{n} \sim -2.8$ and −1.7 × 10^{11} cm^{-2}, respectively. The dV/dI peaks disappear at higher temperatures, which is consistent with an ultra-small Fermi energy of ~1 meV.

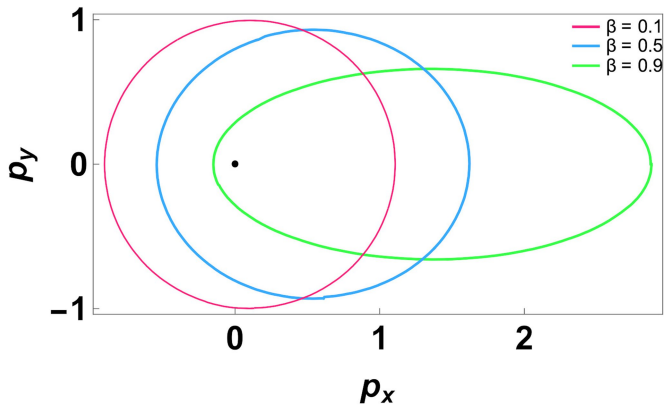

Extended Data Fig. 4 | The shape of Fermi surface in the lab frame for various rescaled drift velocity $\beta = v_n/v_F$. Plot of the Fermi surface for various β versus x and y momentum components p_x and p_y.

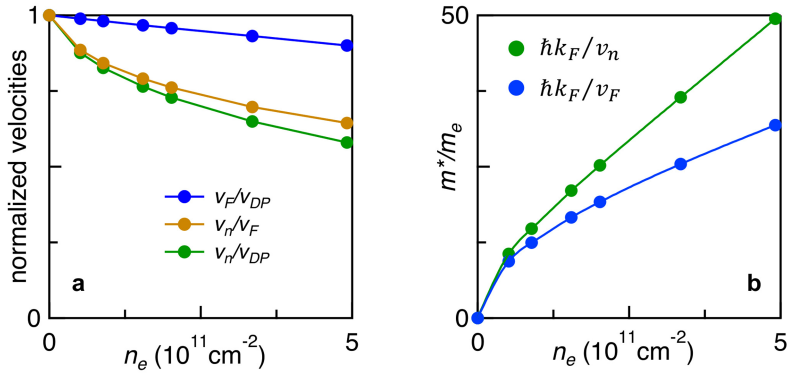

Extended Data Fig. 5 | Theoretical modelling of Fermi velocity v_F and the critical drift velocity v_n. a v_F and v_n in units of the Fermi velocity at the Dirac point v_{DP}, as well as v_n/v_F, versus electron density n_e. **b** the effective masses at Fermi energy, $\hbar k_F/v_F$ in theory and $\hbar k_F/v_n$ in measurements, in units of the bare electron mass m_e as functions of the electron density n_e.

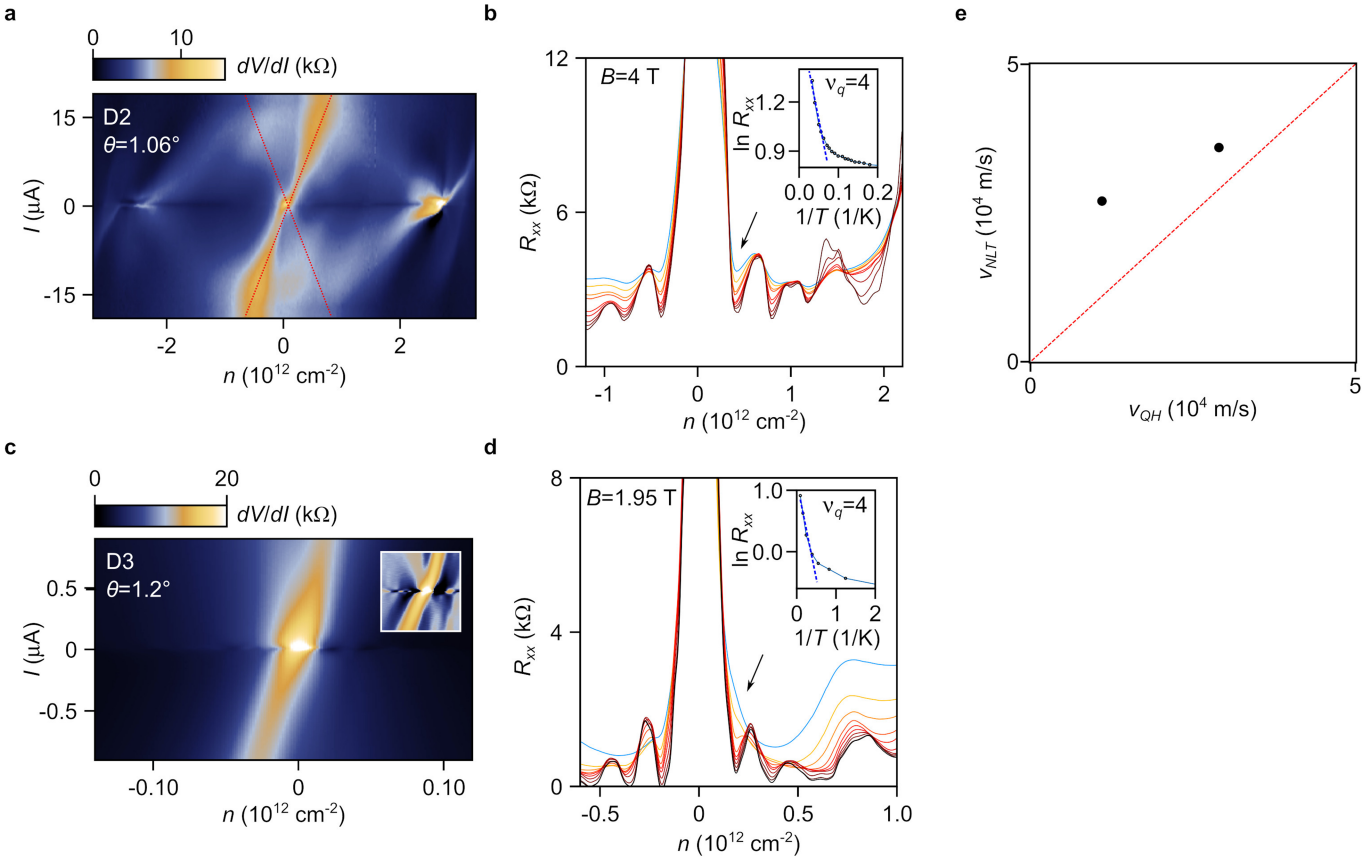

Extended Data Fig. 6 | Comparison between velocity measured from quantum Hall effect, Shubnikov–de Hass oscillations and non-linear transport measurements near charge neutrality. a dV/dI versus density n and bias current I for device D2 with $\theta = 1.06°$. Peaks due to the Schwinger effect are indicated by the red dashed lines. **b** R_{xx} versus n at $T = 30, 25, 20, 18, 12, 10, 7, 5$ and 2.02 K, respectively (blue to black). Inset: Activation plot of R_{xx} measured in the quantum Hall $\nu_q = 4$ valley indicated by the arrow in the main panel taken at $B = 4$ T. **c**–**d** Same as **a**–**b** but for device D3. Inset in **c**: Zoom-in of same data in main panel with background subtracted. Colour scale: black: −1 kΩ; white: 3 kΩ. From blue to black, temperatures in **d** are $T = 10, 6, 4, 2.5, 1.8, 1.2, 0.8, 0.4, 0.1$ and 0.03 K. **e** Plot of v_{QH} versus v_{NLT} for D2 and D3. The dotted line indicates $v_{QH} = v_{NLT}$.

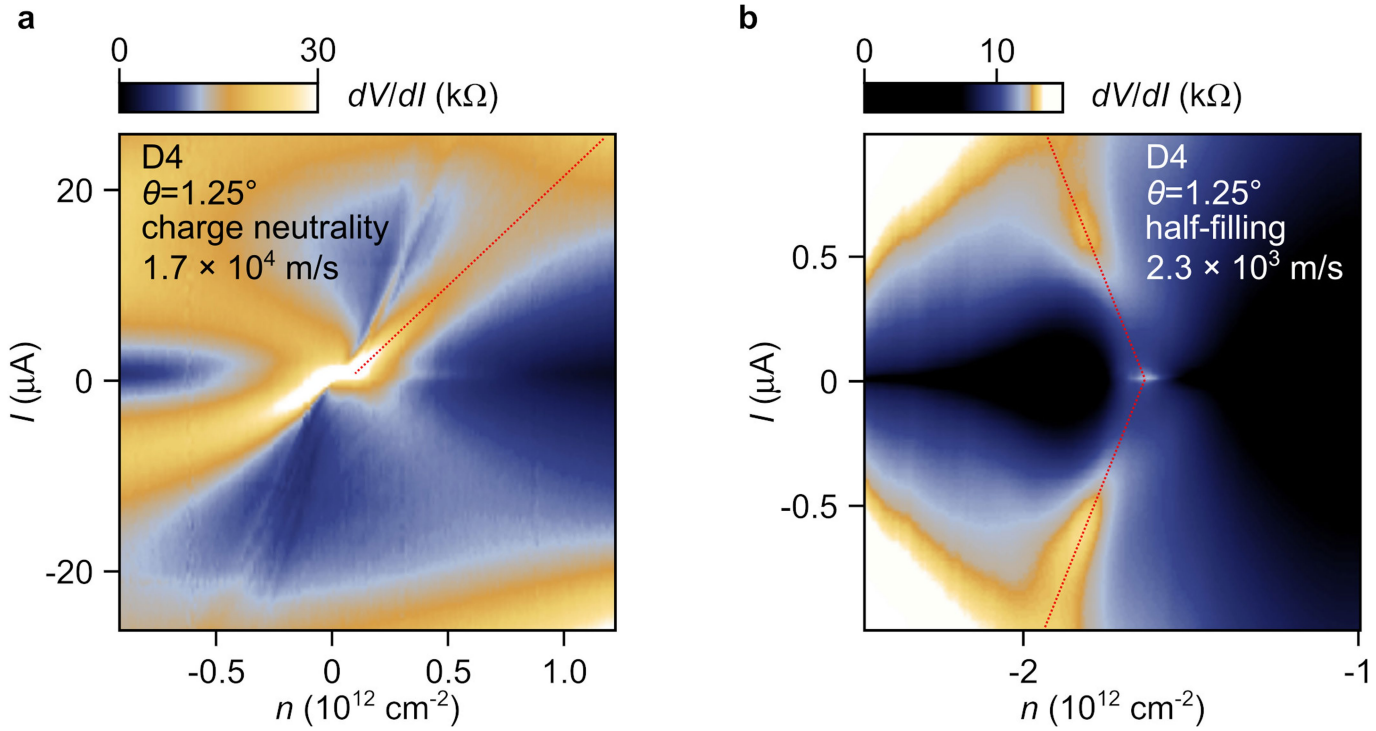

Extended Data Fig. 7 | Non-linear transport data near charge neutrality and half-filling for device D4. a dV/dI (n, I) near charge neutrality. Velocity obtained from slope of features near zero density such as shown by the red dashed line, yielding $v_{NL} = \sim 1.7 \times 10^4$ m s^{-1}; averaging the slopes of features over four quadrants yields $v_{NL} = \sim 1.5 \times 10^4$ m s^{-1}. **b** dV/dI data near half-filling. Features indicated by red dashed lines follow nearly equal slopes, yielding $v_{NL} = 2.3 \times 10^3$ m s^{-1}.

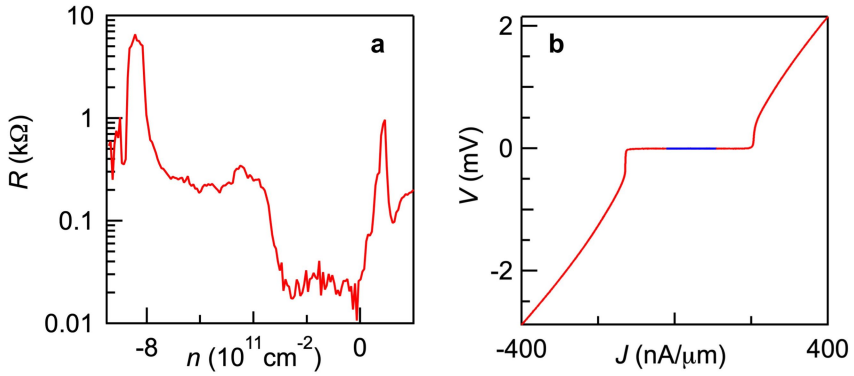

Extended Data Fig. 8 | Comparison of ac and dc measurements. a $R(n)$ at $B = 0$, $T = 0.3$ K and zero bias, measured using ac lock-in techniques with a large dynamic range. The superconducting region displays a "residual" resistance of ~20–30 Ω. **b** DC voltage-current curve at $\tilde{n} = -1.65 \times 10^{11}$ cm^{-2}, $B = 0$ and $T = 0.3$ K. The blue line is a line fit to the zero-bias region, which has a slope of -0.2 ± 1.4 Ω.

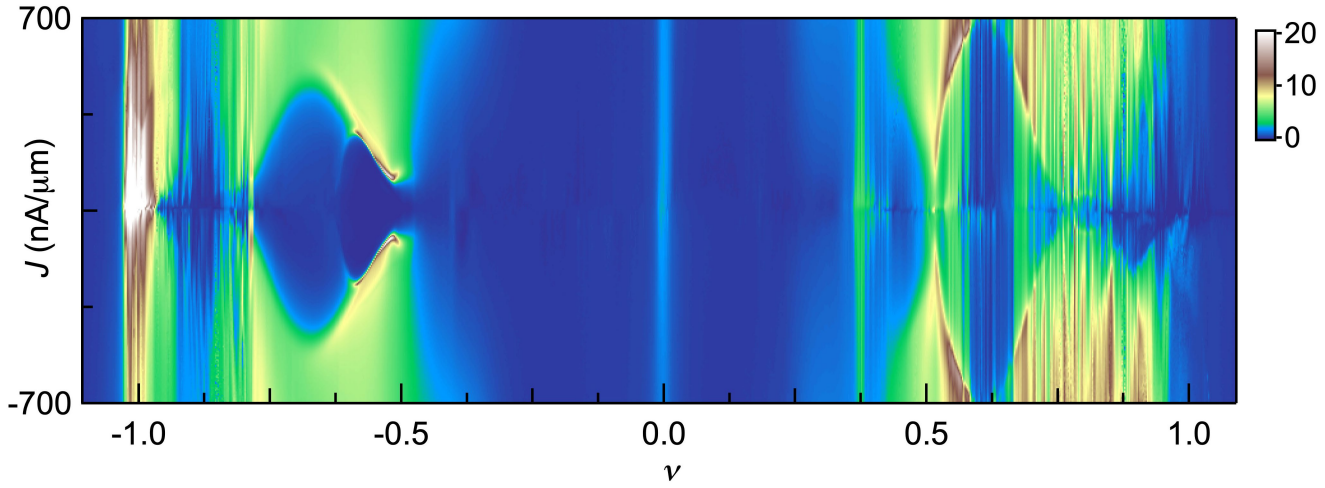

Extended Data Fig. 9 | Transport data over extended range. Nonlinear transport data ***dV/dI*** (***J,ν***) in kΩ over a large density range at ***B*** = 0 and ***T*** = 0.3 K.